GSA Data Repository item 2018135
Appendices DR1-3, Figures DR1-13, Tables DR1-4, and Movie DR1

Supplementary Materials for: B. P. Weiss et al. (2018) Secondary magnetic inclusions in detrital zircons from the Jack Hills, Western Australia and implications for the origin of the geodynamo

Appendix DR1. Paleomagnetism of Jack Hills Rocks

The present study focuses on the remagnetization history of the zircons over the last 4.4 billion years. This goes beyond our previous Jack Hills studies (Weiss et al. 2015; 2016), which examined whether the host rocks for Jack Hills zircons have been remagnetized since deposition at 3.0 Ga. Weiss et al. (2015; 2016) provided evidence that the Jack Hills rocks in the vicinity of the Hadean-zircon discovery outcrop at Erawandoo Hill have been pervasively remagnetized up to peak unblocking temperatures of 320-500°C. They inferred this from 12 baked contact, fold, and conglomerate tests, all of which either failed or were inconclusive. These tests included 3 conglomerate tests on several cm-diameter cobbles from outcrops located several hundred meters northwest and northeast of Erawandoo Hill. These results contrast with a positive cobble conglomerate test conducted at the University of Rochester by Tarduno and Cottrell (2013) and recently augmented with new measurements by Dare et al. (2016) and Bono et al. (2018). Unlike Tarduno and Cottrell (2013), who observed stable NRM unblocking up to the 580°C Curie point of magnetite in most samples, nearly all of the cobbles in Weiss et al. (2015) [as well as cobbles measured at Lehigh University that are reported in Dare et al. (2016); see their Figs. 8b, 9b, S13b, and S14b], show little evidence of stable, origin-trending NRM blocked above the 350°C except when it is apparently carried by hematite or maghemite. The differences between the data acquired at MIT and Lehigh with those from Rochester mean that there is currently no robust evidence that the zircon host rocks have avoided remagnetization since 3.0 Ga.

Unfortunately, the debate about the magnetism of Jack Hills zircons has become mired in minutiae in a way that most readers will find unilluminating. Additionally, a number of the statements by the Rochester group (Dare et al. 2016; Bono et al. 2016; 2018) are unsubstantiated [e.g., that there are "gross...errors in orientation and measurement" of Weiss et al. (2015)'s samples, that there is an "error in field sampling and/or reporting" by Weiss et al. (2015), and that the 12-mm diameter samples of Weiss et al. (2015) are of "insufficient volume…to accurately record…magnetization"; compare with Böhnel et al. (2009), Berndt et al. (2016), and Lima and Weiss (2016)]. Others of their statements are demonstrably false [e.g., that Weiss et al. (2015) "used an Ar atmosphere (B. Weiss, personal communication, 2014)" to thermally demagnetize their samples (they used an air atmosphere and never communicated otherwise to anyone), that Weiss et al. (2015) called for the existence of a "1 Ga overprint…that is seen everywhere" (they never claimed the cobbles have this overprint), and that somehow the fact that the MIT magnetometer is "located high in a tall, narrow building" is relevant for its sensitivity].

As a further example, Dare et al. (2016) and Bono et al. (2018) proposed that the 2G 755 magnetometer at U. Rochester is ~2 orders of magnitude more sensitive than the MIT 2G 755 magnetometer used for the Weiss et al. (2015) study. However, Wang et al. (2017) Fig. S5 showed that of 300 repeat measurements with the MIT magnetometer with no sample in the sense bore, 95% have moments below 9.9×10^{-13} Am^2. This means that the Rochester magnetometer, with a reported sensitivity of $\sim9\times10^{-13}$ Am^2, is at best trivially more sensitive than the MIT magnetometer.

Rather than further prolonging this unfruitful debate, a much more definitive approach would be for the MIT and Rochester laboratories to exchange samples, as we have repeatedly proposed over the last ~4 years (Weiss, 2017; Weiss et al., 2016). Sample exchange would be a straightforward way to test whether differences in the two laboratories' results stem from differences in measurement techniques or in sample magnetizations. We also invite independent, third-party laboratories to make their own measurements, for which we are happy to provide samples. Reproducibility tests like these form the foundation of the scientific method.

Appendix DR2. Measurement Methodology

1. Extraction and preparation of 11 zircon sets. We prepared 11 sets of zircons for magnetic field and compositional measurements (Table DR1). Zircon sets 1 and 2 were extracted from the rocks using a Frantz Model LB-1 Magnetic Separator (during which the grains were exposed to fields up to 1.6 T), washed in alcohol and then dated with U-Pb chronometry following Holden et al. (2009). Sets 3–9 were extracted nonmagnetically using heavy liquids at MIT. Following extraction, some zircons were cleaned with only alcohol while others were treated with HCl in an ultrasonicator with varying concentrations and for varying durations. Prior to magnetic analyses, all but sets 4, 9, and 11 were mounted in nonmagnetic epoxy and polished with alumina to approximately their mid-sections, while sets 4 and 9 were mounted in blind holes in a nonmagnetic glass slide following Fu et al. (2017). Set 10 was U-Pb dated and analyzed using electron microscopy by Bell et al. (2015). Set 11 was analyzed in situ in a 30 µm thin section of the host pebble conglomerate.

2. Quantum diamond microscopy (QDM) Measurements. For the QDM measurements, we used the instrument in vector magnetic microscopy (VMM) mode (Glenn et al., 2017). To extract the vector magnetic fields, we applied a 0.28 mT bias field normal to the diamond chip and 0.44 mT and 1.26 mT fields along the orthogonal transverse directions. We applied these fields in opposite directions in two independent measurements, which we later combined to separate the ferromagnetic and paramagnetic contributions from the zircons. In case of any slight difference between the positive and negative applied fields (which was at most ~0.01 mT), which can result in a uniform offset in the ferromagnetic images, we removed this offset to yield an offset-free ferromagnetic field map.

The noise floor in QDM measurements varies with experimental conditions, including the laser intensity, laser stability, laser polarization, applied microwave field, bias field strength, thermal stability, experiment duration, and diamond chip characteristics (Glenn et al., 2017). For these reasons, some of the QDM maps, particularly those of IRM (e.g., Fig. DR1), have a better noise floor and signal-to-noise ratio than others (e.g., NRM maps in Fig. DR4), Although we aim to maintain optimized sensitivity throughout QDM operation, the magnetic noise floor can vary depending on the above conditions and also on the differing challenges set by each rock sample.

Given the ~500 nT noise floor of the QDM in its high-resolution mode and our measurement height of <10 µm above the polished surface of the zircon, in the best-case scenario (where the magnetic source lies at the polished surface of the zircon), the minimum detectable moment of the zircons 3×10^{-15} Am^2. For an intermediate scenario where the source is buried 30 µm beneath the polished surface, the threshold was 2×10^{-13} Am^2. A zircon with a moment 1×10^{-12} Am^2 moment would be detectable even if the source is 60 µm inside the zircon; because most zircons have diameters of ~100-150 µm, an equivalent dipole at their centers would be detectable.

3. Possibility of contamination. Referring to our initial QDM study of Jack Hills zircons (Glenn et al., 2017), Bono et al. (2018) suggested that the preferential location of magnetization at the edges of our set 1 zircons may be due to contamination within our epoxy mounts or from polishing these mounts. The most compelling reason such contamination is unlikely for the vast majority of our set 1 zircons is that magnetic Fe-rich rinds were not observed around Bishop Tuff zircons (Fu et al., 2017) prepared and analyzed using techniques similar to those here. Here we provide additional analyses that support this conclusion.

With respect to contamination from polishing, our high resolution backscattered electron microscopy (BSEM) and wavelength dispersive spectroscopy (WDS) maps of selected zircon rims show that the secondary Fe-rich materials do not have a composition or texture resembling that of our polishing grits, which were alumina and diamond with grain sizes of 0.1-1 µm (Figs. DR2, 6).

To assess the frequency of contaminants in the epoxy, we consider the 78 zircons from set 1 (i.e., non-acid-washed) imaged in the high-resolution QDM mode (Fig. DR4C-D, G-L). The total area imaged by these maps is 9.87 mm^2 above the epoxy only and 1.95 mm^2 above zircons. The mean area per zircon is 0.024 mm^2 with a standard deviation of 0.006 mm^2. The total number of unambiguous contamination dipoles associated with the epoxy is 11. Assuming a Poisson process for magnetic contaminants falling on the sample with rate $k = 1.11$ mm^{-2}, then a typical zircon (area $A = 0.024$ mm^2) has a probability $P = 1 - \exp(kA) = 0.026$ to have one or more contamination dipoles land on top of it. The expected number of contamination dipoles over all zircons is $N_{tot} = 1.11$ mm^{-2} × 1.95 mm^2 = 2.2. Given that there are hundreds of dipoles over the 78 zircons, contamination associated with the epoxy mount is extremely unlikely to explain the magnetization at the edges of most zircons.

Appendix DR3. Comparison with Inclusion Study of Bell et al. (2015)
We briefly discuss our results in light of the Jack Hills zircon inclusion study by Bell et al. (2015). Drawing on their dataset, we find that of the 68 zircons they found to contain Fe oxides, just 6 (9%) contain Fe oxides not obviously associated with cracks or healed cracks, with the remainder clearly associated with these secondary textures (Fig. DR13). Raman spectroscopy showed that an Fe oxide inclusion in the crack of a Hadean grain (RSES77–5-7) is hematite. On the other hand, 5 of the 6 zircons found to have interior Fe oxides isolated from cracks and voids (making up 7% of the population), our energy dispersive spectroscopy (EDS) and cathodoluminescence (CL) analyses did not identify any Fe oxides in cracks or voids, meaning that there is a small population of Jack Hills zircons that may be candidates for containing ferromagnetic minerals that are dominantly primary. However, these grains may contain Fe oxides hidden in cracks and that are not exposed at the polished surface.

Figure DR1. Maps of the magnetization, texture and composition of Jack Hills zircons from set 1 (i.e., not acid-washed) other than those shown in Fig. 1. Shown are quantum diamond microscopy (QDM) maps of the out-of-the-plane component of the isothermal remanent magnetization (IRM) magnetic field superimposed on backscattered electron microscopy (BSEM) images (left), BSEM images (middle), and maps of Fe abundance from wavelength dispersive spectroscopy (right). Zircon in (A)-(J) have interior magnetic sources only, those in (K)-(L) did not have any detectable magnetic sources, and those in (N-O) have interior magnetic sources. (A) RSES199-1-17: Pb-Pb age of <3900 Ma. (B) RSES199-2-14 (Pb-Pb age of <3900 Ma). (C) RSES 199-2-17 (Pb-Pb age of <3900 Ma). (D) RSES 199-3-15 (Pb-Pb age <3900 Ma). Higher resolution BSEM and WDS data for boxed region are show in Fig. DR2. (E) RSES 199-3-17 (Pb-Pb age 3954 ± 9 Ma). (F) RSES 199-10-3 (Pb-Pb age <3900 Ma). (G) RSES 199-13-2 (Pb-Pb age 4189 ± 20 Ma). (H) RSES 199-14-3 (Pb-Pb age 4100 ± 10 Ma). (I) RSES 199-2-15 (Pb-Pb age <3900 Ma). (J) RSES 199-2-16 (Pb-Pb age 4053 ± 6 Ma). (K) RSES 199-9-9 (Pb-Pb age <3900 Ma). (L) RSES 199-10-1 (Pb-Pb age <3900 Ma). (M) RSES 199-1-14 (Pb-Pb age <3900 Ma). (O) RSES 199-12-2 (Pb-Pb age <3900 Ma). (P) RSES 199-4-17 (Pb-Pb age <3900 Ma). See Fig. DR3 for QDM data on all set 1 zircons. See Table DR4 for the Pb-Pb ages of these zircons.
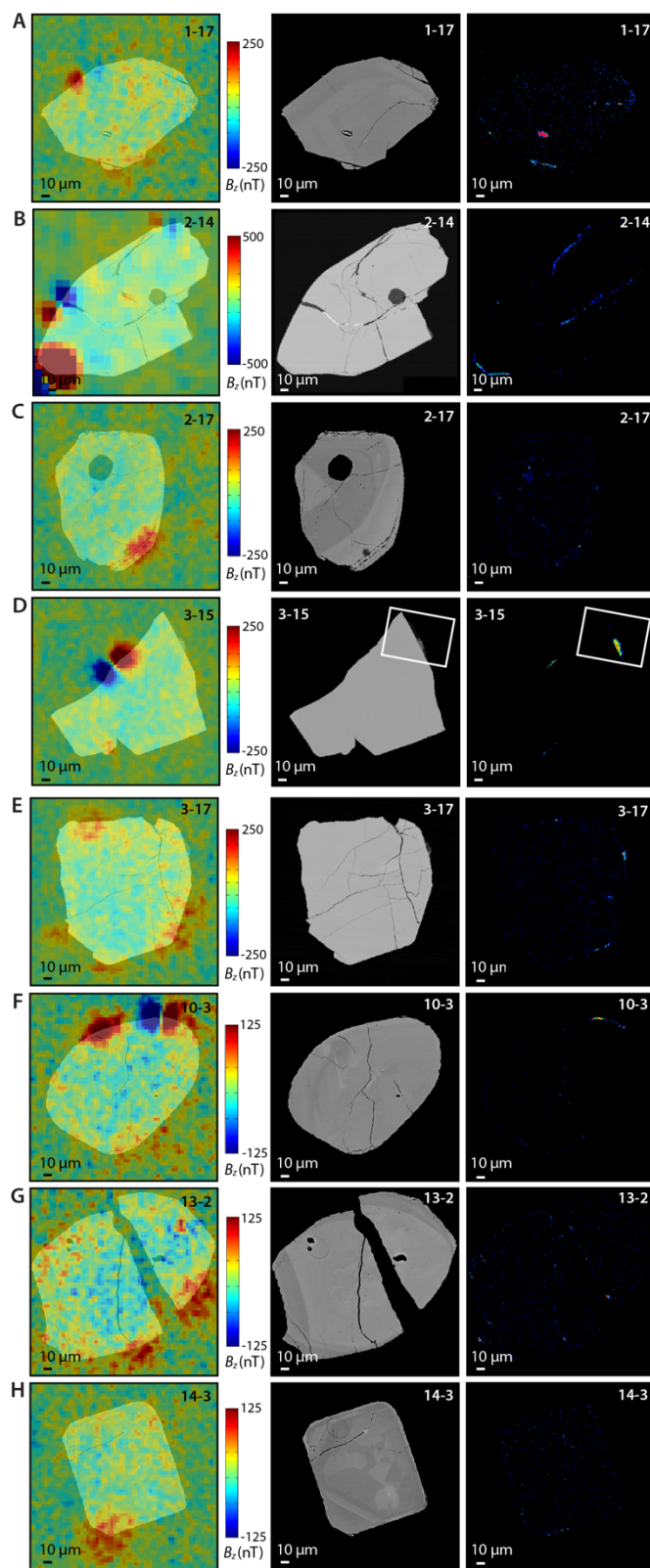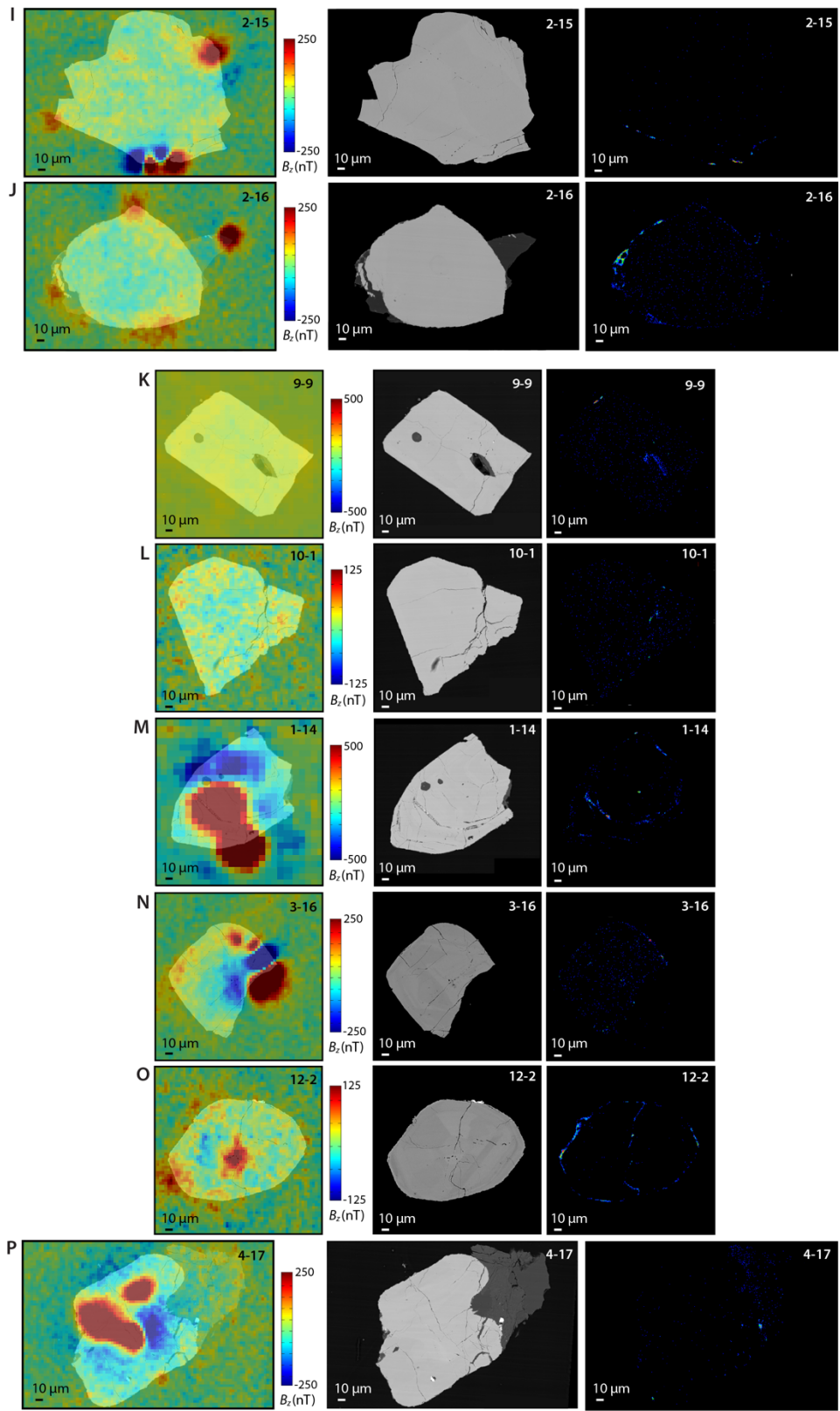
Fig DR2. High-resolution and multi-element electron microscopy analyses of Fe-rich rim on set 1 (i.e., non-acid washed) Jack Hills zircon RSES199-3-15 (see Fig. DR1D). (A) Backscattered electron microscopy (BSEM) image. White polygon shows location of measurements shown in (B-G). (B) BSEM image of polygon-shaped region. (C-G) Wavelength dispersive spectroscopy maps of Zr (C), F (D), Al (E), Si (F), and K (G). Note that he composition and texture of this rind are inconsistent with that of the 1 μm diamond grit used to polish our samples [e.g., Bono et al. (2018)].

A BSEM

10 μm

B BSEM **C** Zr

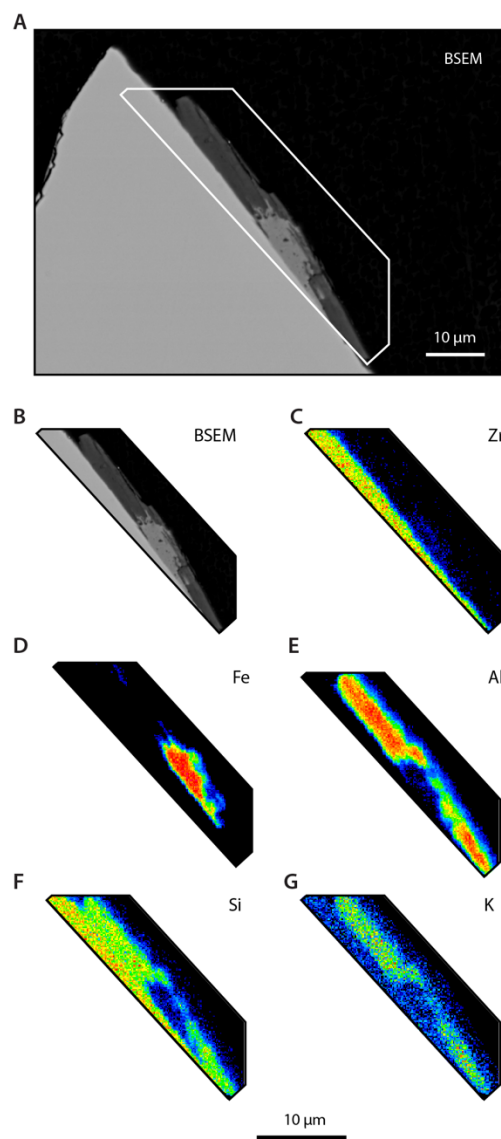**D** Fe **E** Al

F Si **G** K

10 μm

Figure DR3. QDM imaging of the IRM magnetic fields of all Jack Hills zircons analyzed from set 1. (A) Reflected light image of a matrix of zircons from the Jack Hills of Western Australia, polished and embedded in epoxy. Black boxes show fields-of-view imaged with QDM in (B-L). (B-L) Out-of-the-plane component of the magnetic field superimposed on reflected light image for corresponding fields-of-view in (A). Maps in (B, E, F, M) were acquired in the low-resolution mode, while the remaining maps were acquired with the high-resolution mode (see Appendix DR2). QDM maps were acquired at a height of 1-10 µm above the disk. As shown in four corners of each panel, zircons are identified with a two-digit code with their row number followed by their column number, with the zircon in row 1 and column 1 located at the uppermost left position on the epoxy mount and the zircon in row 1 and column 20 located at uppermost right position on the mount. Additional electron microscopy and X-ray tomography data were acquired for the following zircons: (B) Zircon 1-14 (see Fig. DR1M) and zircon 2-14 (see Fig. DR1B). (C) Zircon 1-15 (see Fig. 2), zircon 1-16 (see Fig. DR1E), zircon 1-17 (see Fig. DR1A), zircon 2-15 (see Fig. DR1I), zircon 2-16 (see Fig. DR1J), zircon 2-17 (see Fig. DR1C), zircon 3-15 (see Figs. DR1D and DR2), zircon 3-16 (see Fig. DR1N), zircon 3-17 (see Fig. DR1E), zircon 4-15 (see Fig. 1A), zircon 4-16 (see Fig. 1B), and zircon 4-17 (see Fig. DR1P). (G) Zircon 10-1 (see Fig. DR1L), zircon 10-2 (see Fig. 1B), zircon 10-3 (see Fig. DR1F), and zircon 12-2 (see Fig. DR1O). (J) Zircon 9-9 (see Fig. DR1K). (L) Zircon 13-2 (see Fig. DR1G), zircon 13-3 (see Fig. 1D), and zircon 14-3 (see Fig. DR1H). Circled zircons have Pb-Pb ages >3.9 Ga and uncircled ages have younger Pb-Pb ages. See Table DR4 for the Pb-Pb data for these zircons. Scale bars for are 300 µm.

B

1-12　　　　　　　　1-20

9-12　　　　　　　　9-20

B_z(nT)
500
−500

C

1-15　　1-17

4-15　　4-17

B_z(nT)
250
−250

D

1-18　1-19

4-18　4-19

B_z(nT)
1000
−1000

>3.9 Ga　　300 μm

A

1-1　　　　　　　　　　　1-20

B
C　D
F
E
I
J　K
G　H
L
M

20-1　　　　　　　　　　　20-20

300 μm

E

7-1　　　　　　　　7-9

15-1　　　　　　　　15-9

B_z(nT)
500
−500

F

7-10　　　　　　　　7-18

15-10　　　　　　　　15-18

B_z(nT)
500
−500

G

9-1　　9-3

12-1　　12-3

B_z(nT)
125
−125

H

9-5　　9-8

12-5　　12-8

B_z(nT)
125
−125

I

8-8　　8-9

11-8　　11-9

B_z(nT)
1000
−1000

J

8-9　　　　8-12

11-9　　　　11-12

B_z(nT)
500
−500

K

8-12　　8-13

11-12　　11-13

B_z(nT)
1000
−1000

L

13-2　　13-4

16-2　　16-4

B_z(nT)
125
−125

M

11-12　　　　　　　11-20

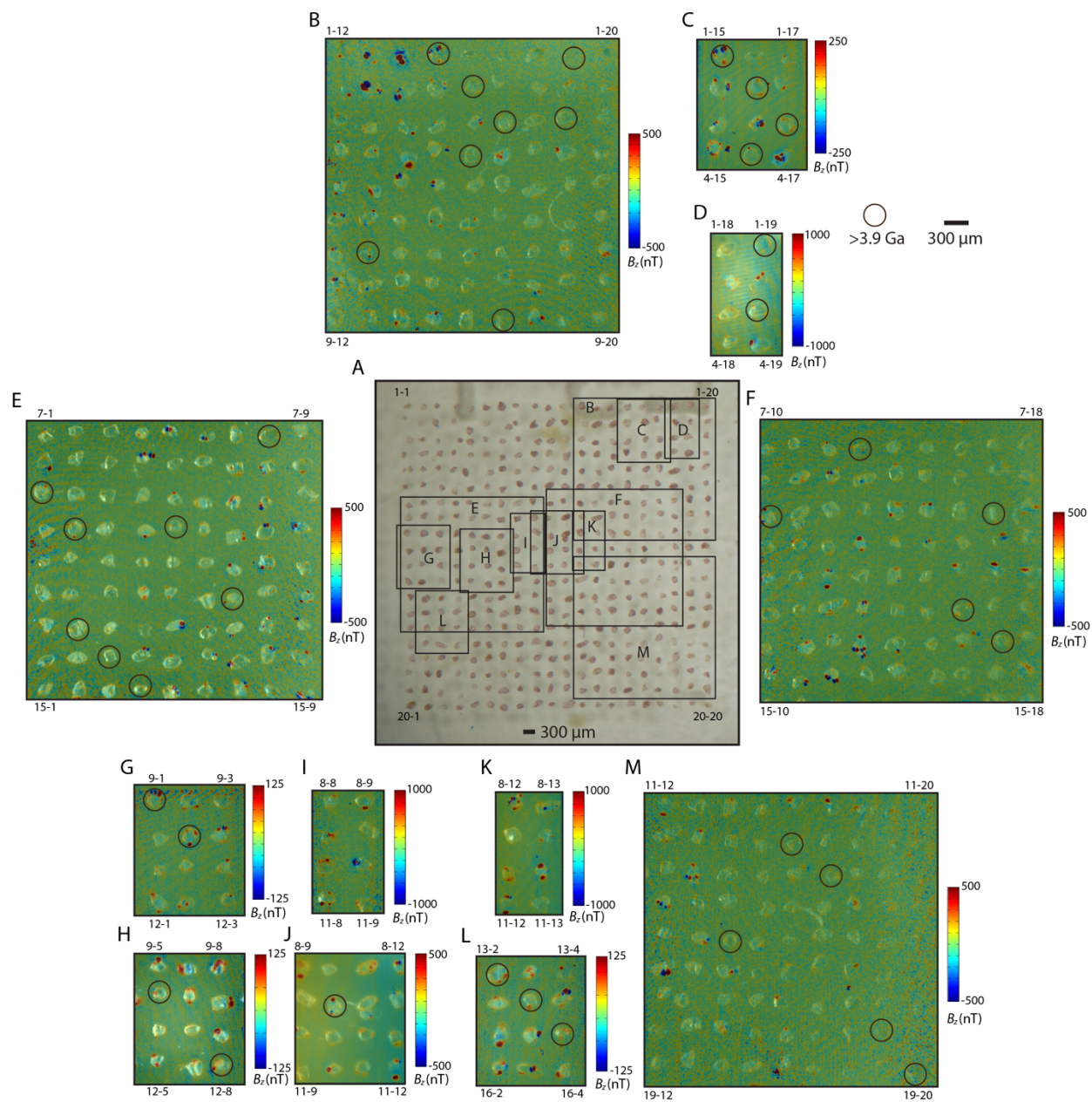19-12　　　　　　　19-20

B_z(nT)
500
−500

11

Figure DR4. QDM imaging of the magnetic fields of Jack Hills zircons carrying natural remanent magnetization (NRM) in sets 3 (i.e., not acid-washed) and sets 5 and 6 (i.e., washed in 0.5 N HCl for 2 and 20 h, respectively). Shown are maps out-of-the-plane component of the magnetic field superimposed on transmitted light images of each zircon. QDM maps were acquired at a height of 1-10 μm above the disk. Zircons in (A-D) are from set 3, those in (E-G) are from set 5 and those in (H-J) are from set 6. See Figs. DR5-6 for compositional maps of some of the set 6 zircons shown here. Scale bar is 100 μm. (A) Zircons D175M-A1-1-1 (top) and D175M-A1-2-1 (bottom). (B) Zircons D175M-A1-1-1 (top left), D175M-A1-2-1 (bottom left), D175M-A1-1-2 (top right), and D175M-A1-2-2 (bottom right). (C) Zircons D175M-A1-5-2 (top) and D175M-A1-6-2 (bottom). (D) Zircons D175M-A1-4-3 (top) and D175M-A1-5-3 (bottom). (E) Zircons D175M-A2-4-4 (top) and D175M-A2-5-4 (bottom). (F) Zircons D175M-A2-6-4 (top) and D175M-A2-7-4 (bottom). (G) Zircons D175M-A2-4-5 (top) and D175M-A2-5-5 (bottom). (H) Zircons D175M-A3-4-6 (top) and D175M-A3-5-6 (bottom). (I) Zircons D175M-A3-5-7 (top) and D175M-A3-6-7 (bottom). (J) Zircons D175M-A3-5-8 (top) and D175M-A3-6-8 (bottom).
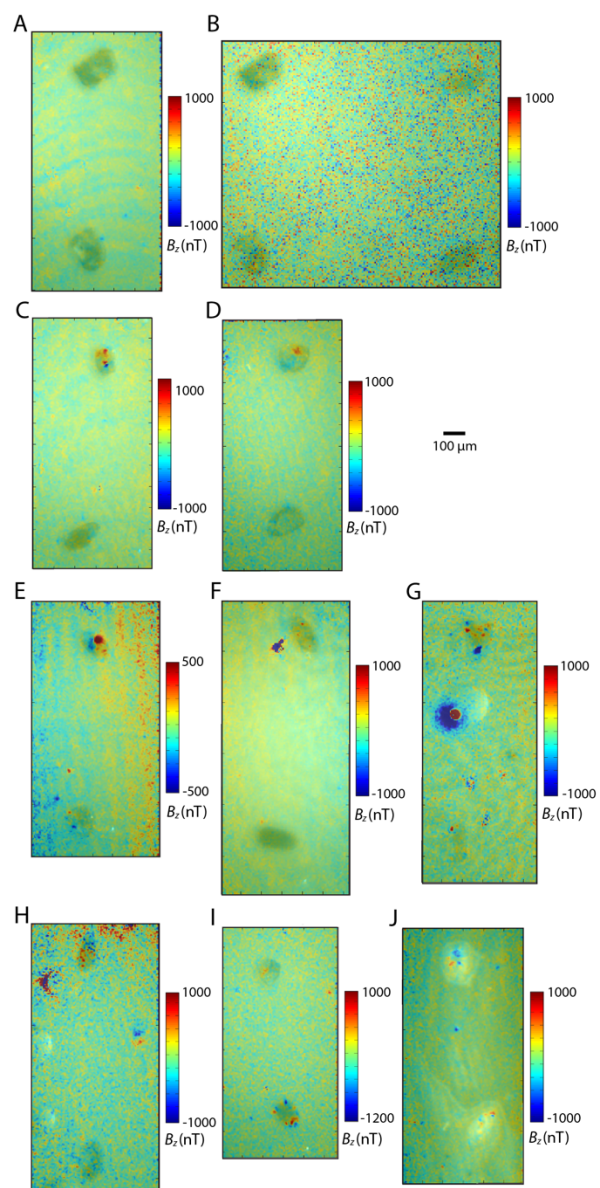
Figure DR5. SEM maps of the magnetization, texture and composition of Jack Hills zircons from set 6 (i.e., treated with 0.5 N HCl for 20 h). (A) Zircon D175M-A3-6-7. (B) Zircon D175M-A3-6-8. See Fig. DR4 for QDM maps of zircons analyzes from sets 3, 5, and 6. Higher resolution BSEM and WDS data for boxed region are show in Fig. DR6.
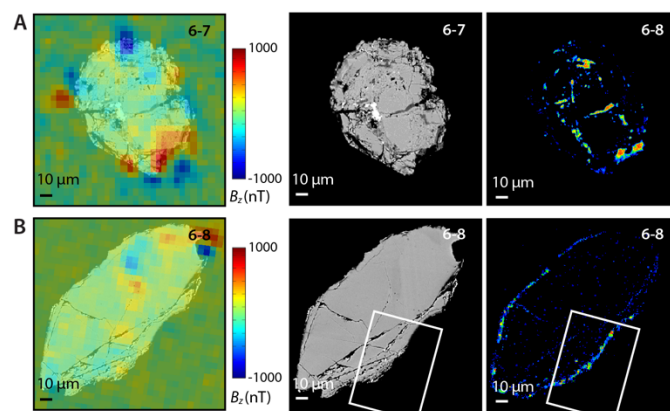
Figure DR6. High-resolution and multi-element electron microscopy analyses of Fe-rich rim on set 6 (i.e., treated with 0.5 N HCl for 20 h) Jack Hills zircon D175M-A3-6-8 (see Fig. DR5B). (A) Backscattered electron microscopy (BSEM) image. White polygon shows location of measurements shown in (B-G). (B) BSEM image of polygon-shaped region in (A). (C-G) Wavelength dispersive spectroscopy maps of Zr (C), F (D), Al (E), Si (F), and O (G). Note that he composition and texture of this rind is inconsistent with that of the 0.1-1 μm alumina (Al_2O_3) grit used to polish our samples [e.g., Bono et al. (2018)].

A BSEM

10 µm

B BSEM

C Zr

D Fe
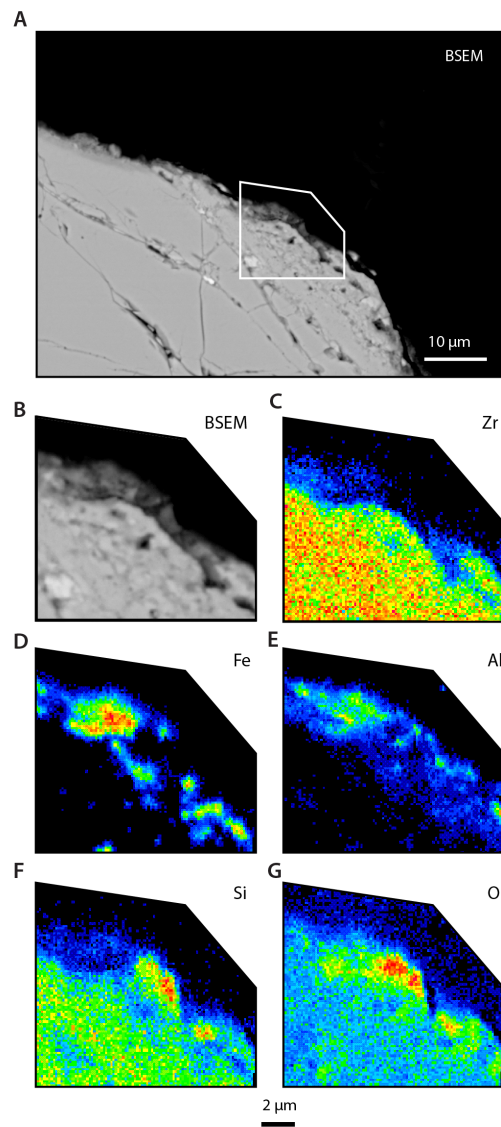
E Al

F Si

G O

2 µm

Figure DR7. Analysis of detrital zircons in situ in a 30 µm thin section of the Erawandoo Hill quartz pebble conglomerate. Although some zircons have weak magnetic anomalies, most of the magnetization is associated with the boundaries between quartz grains. (A, B) QDM maps of the out-of-the-plane component of the IRM magnetic field superimposed on transmitted light crossed polar photomicrographs. Most grains are quartz, but grain boundaries commonly have secondary minerals including clays and Fe oxides. Zircons are identified with arrows. The heights of panels (A) and (B) are each ~700 µm, meaning they are each similar in size to the single microconglomerate test samples in the study of Tarduno et al. (2015). (C, D) BSEM images of the boxed regions in (A) and (B), respectively. The magnetic anomalies in (A, B) are shown to commonly correspond with cracks and alteration textures.

A

zircon
zircon
quartz
zircon
zircon
clay
quartz

0.1 mm

B

quartz
zircon
quartz

B_z(nT)
1000
-1000

0.1 mm

C

0.1 mm

D

0.1 mm

19

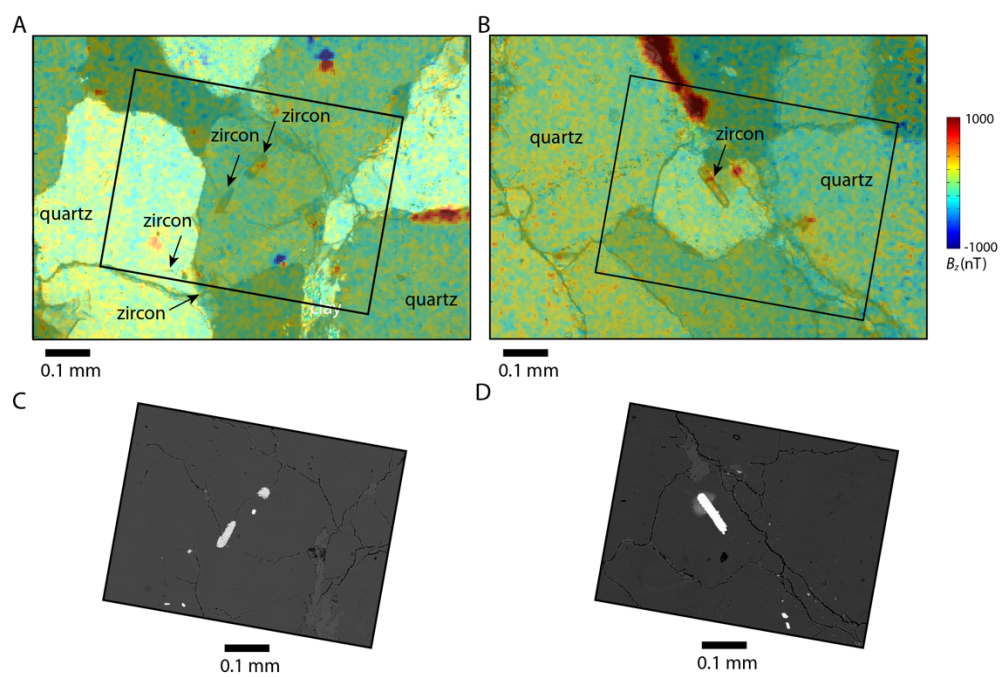**Figure DR8.** (A) Raman spectrum of zircon RSES 57-2-13 (Pb-Pb age 4016 ± 6 Ma). The zircon exhibits peaks at wavenumbers corresponding to those of zircon (Nasdala et al., 1995) (blue) and hematite (red) standards (de Faria and Lopes, 2007). (B) Transmitted light photomicrograph of zircon showing location where Raman spectrum was acquired (white circle). The image is approximately 0.3 mm across.
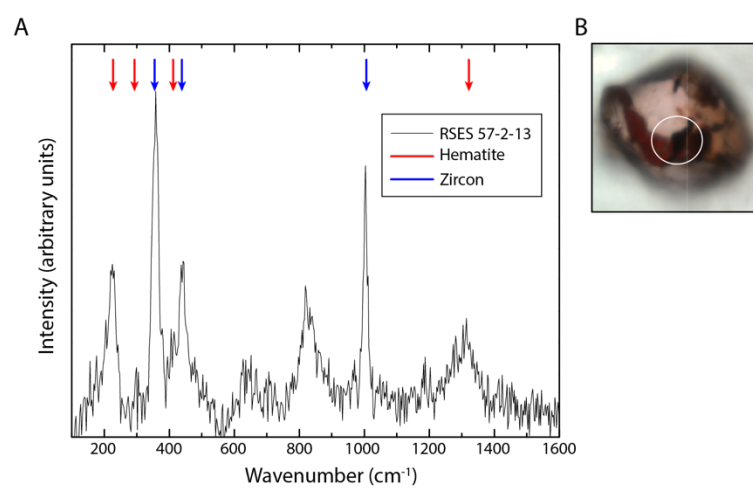
A

B

Figure DR9. Thermal demagnetization data for non-acid-washed Jack Hills zircons carrying IRM (i.e., set 2) not shown in Fig. 3. Shown is the magnetic moment inferred from SQUID microscopy (SM) maps following each thermal demagnetization step (0°C denotes no heating). Red points indicate a second thermal demagnetization of IRM experiment conducted after the zircons had been heated to 680°C. Blue points equal the IRM intensity after two repeat thermal demagnetization experiments to 680°C. Zircons in (A-F) are inferred to all contain hematite (Curie temperature 675°C) with some also containing goethite (Curie temperature 50-120°C). Zircon in (G) is inferred to contain both hematite and magnetite (Curie temperature 580°C), while zircon in (H) has uncertain magnetic mineralogy. All zircons except those in (D) and (H) were found to contain origin-trending, single-component IRMs; the two-component magnetization in zircon in (D) likely results from the fact that our 400 mT IRM did not completely overprint the <1.6 T IRM from the Frantz. Dashed lines indicate demagnetization steps in which the magnetic moment no longer exhibits directional coherence in orthographic projection plots. (A) Zircon RSES 57-9-19 (Pb-Pb age <3900 Ma). (B) Zircon RSES 57-1-3 (Pb-Pb age 4039 ± 7 Ma). (C) Zircon RSES 57-4-15 (Pb-Pb age <3900 Ma). (D) Zircon RSES 57-3-19 (Pb-Pb age <3900 Ma). (E) Zircon RSES 57-19-20 (Pb-Pb age <3900 Ma). Note that this zircon's magnetization direction remains within 50° of the original undemagnetized IRM direction until the final demagnetization step of 674°C. (F) Zircon RSES 57-15-11 (Pb-Pb age 4048 ± 9 Ma). (G) Fragment A of zircon RSES 57-6-19 (Pb-Pb age <3900 Ma). Thermal demagnetization of another fragment of this zircon is shown in Fig. 3A. (H) Zircon RSES 57-19-12 (Pb-Pb age 4124 ± 6 Ma). See Table DR4 for the Pb-Pb data for these zircons.

Hematite- and Goethite-Bearing

Hematite- and Magnetite-Bearing

Ambiguous

A
goethite *pyrrhotite* *magnetite* *hematite*
Moment (×10⁻¹² Am²)
<3900 Ma
zircon RSES 57-9-19
Temperature (°C)

B
goethite *pyrrhotite* *magnetite* *hematite*
Moment (×10⁻¹² Am²)
4039 Ma
zircon RSES 57-1-3
After heating once
Temperature (°C)

C
Moment (×10⁻¹³ Am²)
<3900 Ma
zircon RSES 57-4-15
After heating once
After heating twice
Temperature (°C)

D
Moment (×10⁻¹³ Am²)
<3900 Ma
zircon RSES 57-3-19
Temperature (°C)

E
Moment (×10⁻¹³ Am²)
<3900 Ma
zircon RSES 57-19-20
Temperature (°C)

F
goethite *pyrrhotite* *magnetite* *hematite*
Moment (×10⁻¹³ Am²)
4048 Ma
zircon RSES 57-15-11
Temperature (°C)

G
Moment (×10⁻¹² Am²)
<3900 Ma
zircon RSES 57-6-19A
Temperature (°C)

H
Moment (×10⁻¹³ Am²)
4124 Ma
zircon RSES 57-19-12
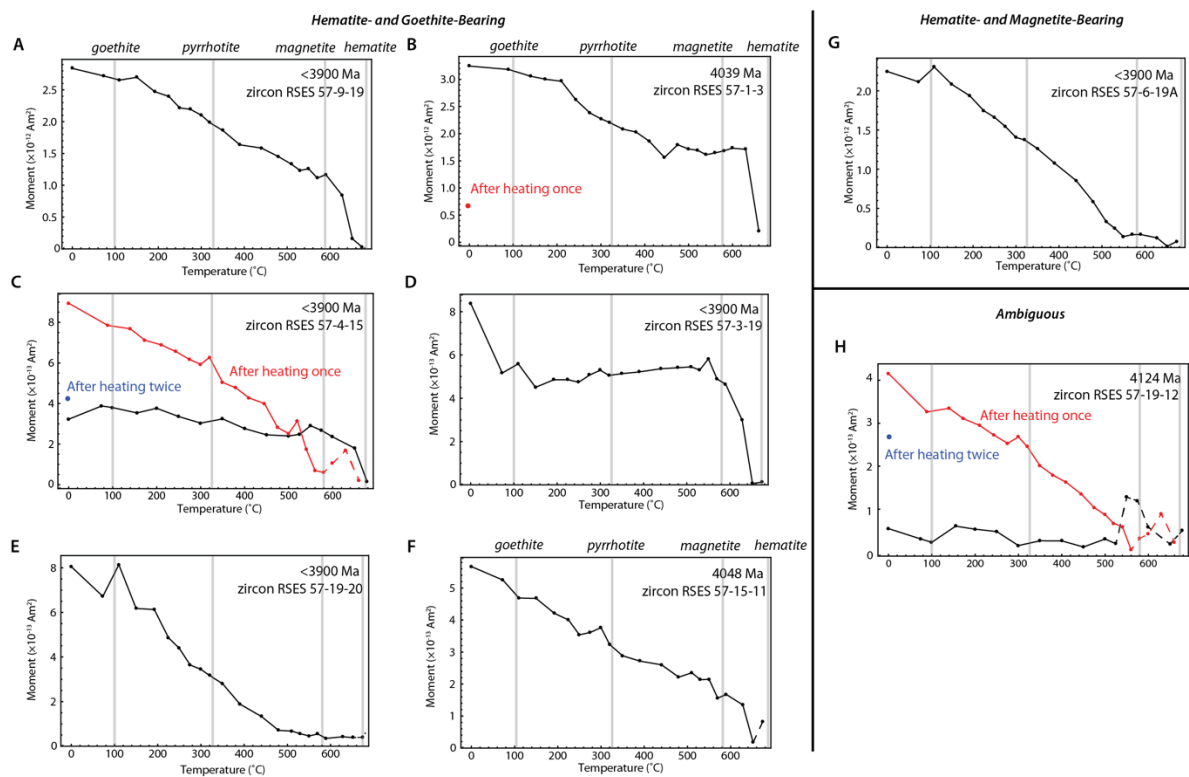After heating once
After heating twice

Figure DR10. SM maps of the NRM of zircons from sets 4 (i.e., non-acid-washed) and set 9 (washed with 6 N HCl for 12 minutes) mounted in two polished epoxy disks. Shown is the vertical component of the magnetic at a height of 170 μm above the disk. (A) Set 4. (B) Set 9.
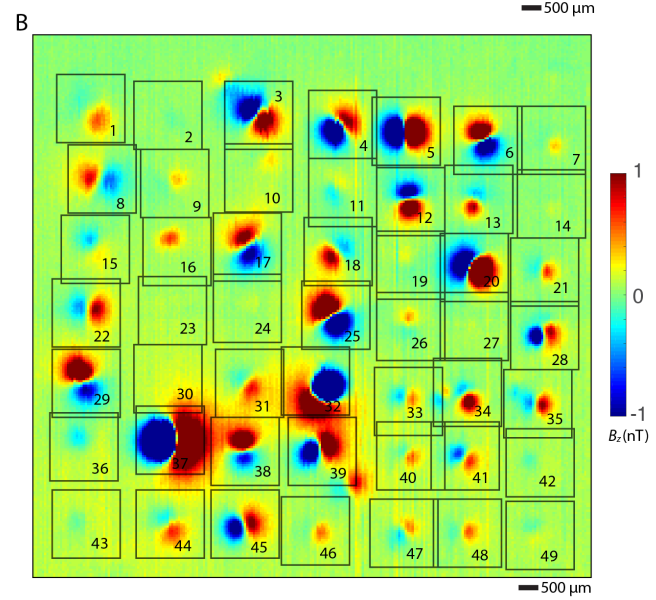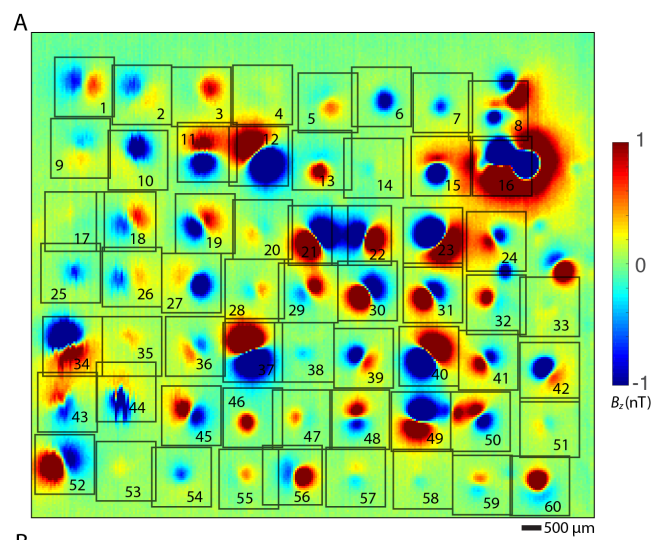
A

B

B_z(nT)

500 μm

Figure DR11. Maps of magnetization, texture and composition of Jack Hills zircons washed with 6 N HCl for 12 minutes (i.e., set 7) and 1 h (i.e., set 8) not shown in Fig. 4. Shown are QDM maps of the out-of-the-plane component of the IRM magnetic field superimposed on BSEM images (left), BSEM images (middle), and maps of Fe abundance from wavelength dispersive spectroscopy (right). (A) Zircon D175M-B1-4-2. (B) Zircon D175M-B1-4-1. (C) Zircon D175M-B1-3-2. (D) Zircon D175M-B2-1-4. (E) Zircon D175M-B2-2-5. (F) Zircon D175M-B2-3-5. (G) Zircon D175M-B1-3-1. (H) Zircon D175M-B2-1-5.

A 4-2 4-2 4-2
10 µm 10 µm 10 µm

B 4-1 4-1 4-1
10 µm 10 µm 10 µm

C 3-2 3-2 3-2
10 µm 10 µm 10 µm

D 1-4 1-4 1-4
10 µm 10 µm 10 µm

E 2-5 2-5 2-5
10 µm 10 µm 10 µm

F 3-5 3-5 3-5
10 µm 10 µm 10 µm

G 3-1 3-1 3-1
10 µm 10 µm 10 µm

H 1-5 1-5 1-5
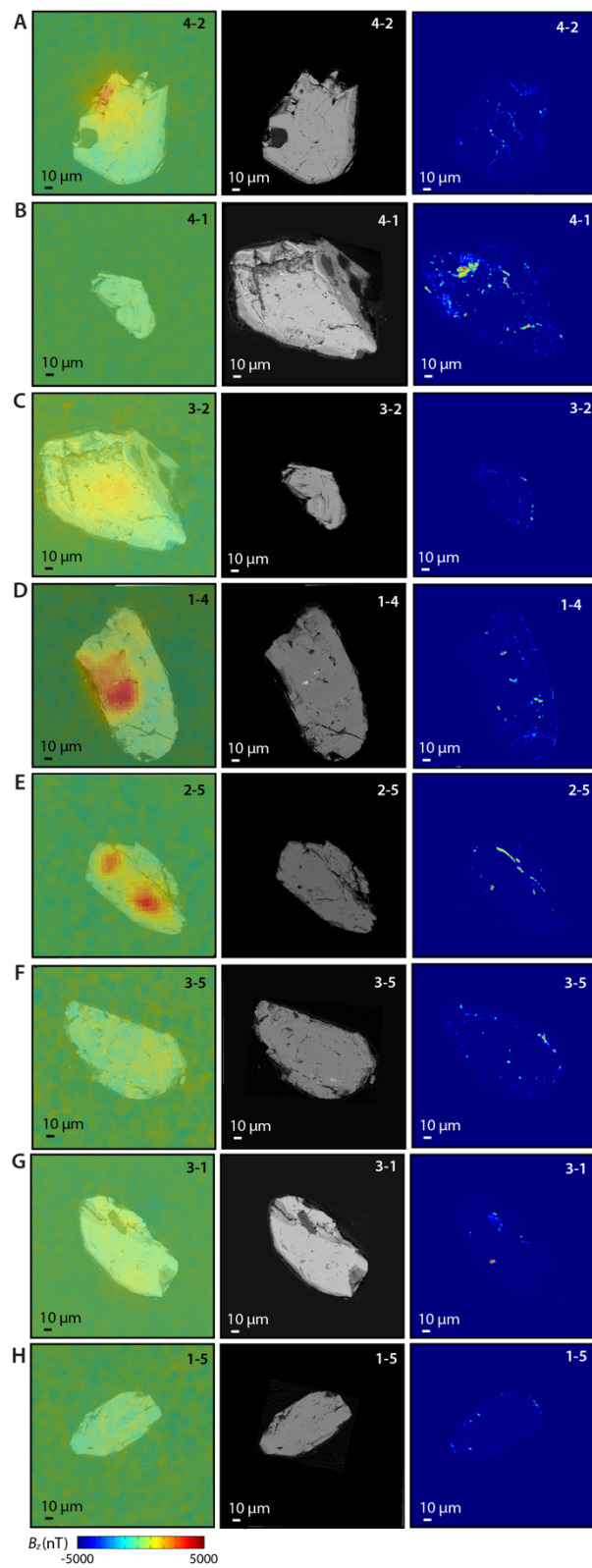10 µm 10 µm 10 µm

B_z (nT)
-5000   5000

Figure DR12. QDM imaging of the IRM magnetic fields of all Jack Hills zircons from sets 7 (i.e., washed in 6 N HCl for 12 min) and 8 (i.e., washed in 6 N HCl for 1 h). Shown are maps out-of-the-plane component of the magnetic field superimposed on transmitted light images of each zircon. QDM maps were acquired at a height of 1-10 μm above the disk. Zircons in (A-B), (F-H), and (J-L) are from set 7 and those in (C-E), (I), and (M-N) are from set 8. See Figs. 4 and DR11 for compositional maps of some of the zircons shown here. Scale bar is 100 μm. Sets 7 and 8 were mounted on one epoxy disk; the maps are arranged such that the zircons are in the same approximate locations that they have on the epoxy disk. (A) Zircons D175M-B1-1-1 (top) and D175M-B1-2-1 (bottom). (A) Zircons D175M-B1-1-2 (top) and D175M-B1-2-2 (bottom). (C) Zircons D175M-B1-1-4 (top) and D175M-B2-2-4 (bottom). (D) Zircons D175M-B2-1-5 (top) and D175M-B2-2-5 (bottom). (E) Zircons D175M-B2-1-6 (top) and D175M-B2-2-6 (bottom). (F) Zircons D175M-B1-3-1 (top) and D175M-B1-4-1 (bottom). (G) Zircons D175M-B1-3-2 (top) and D175M-B1-4-2 (bottom). (H) Zircons D175M-B1-3-3 (top) and D175M-B1-4-3 (bottom). (I) Zircons D175M-B2-3-5 (top) and D175M-B2-4-5 (bottom). (J) Zircons D175M-B1-4-1 (top) and D175M-B1-5-1 (bottom). (K) Zircons D175M-B1-4-2 (top) and D175M-B1-5-2 (bottom). (L) Zircons D175M-B1-4-3 (top) and D175M-B1-5-3 (bottom). (M) Zircons D175M-B2-4-4 (top) and D175M-B2-5-4 (bottom). (M) Zircons D175M-B2-4-5 (top) and D175M-B2-5-5 (bottom).
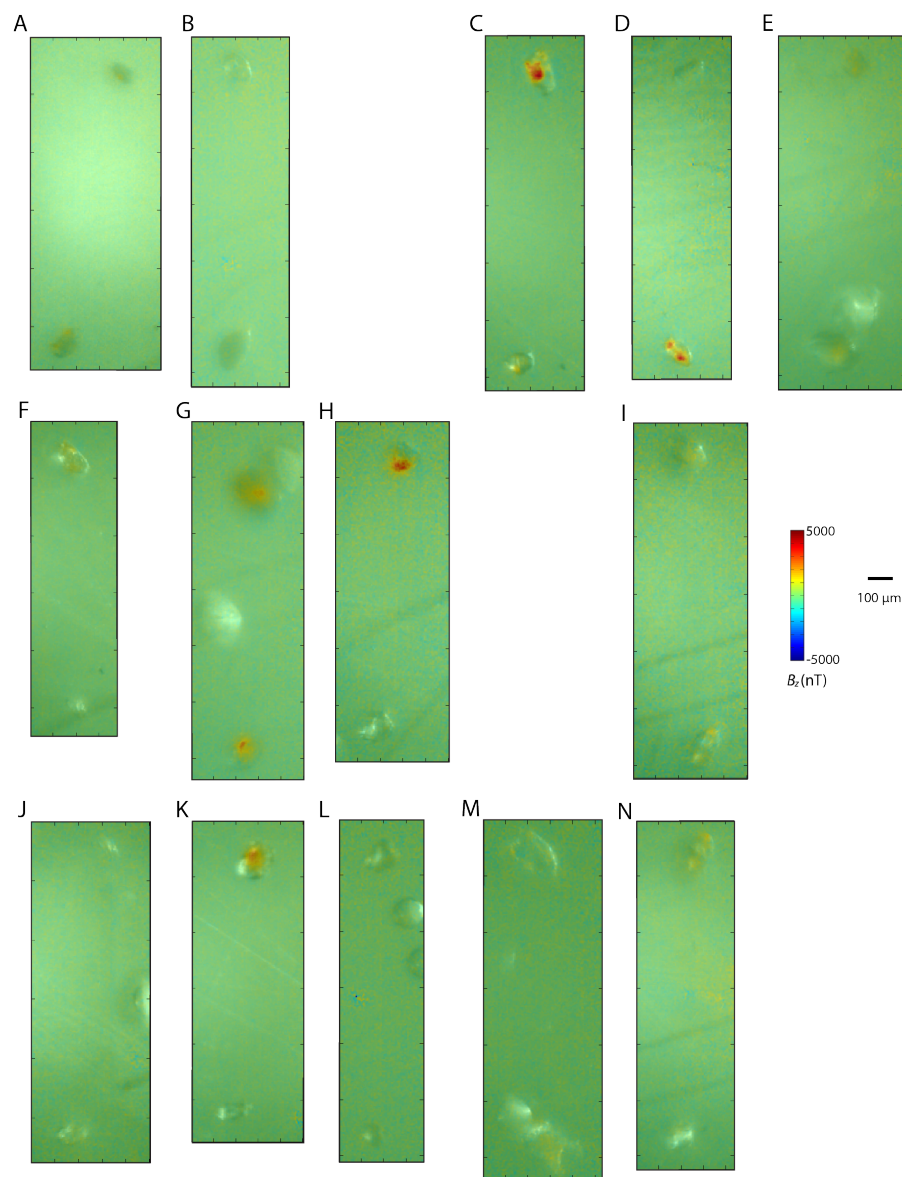
Figure DR13. The association of secondary textures and Fe oxides in Jack Hills zircons. Shown are examples of zircons intersected by cracks [(A), top iron oxide in (B) and large Fe oxide at bottom left of (F)], filling cracks [bottom Fe oxide in (B)], filling cracks (C), intersected by annealed cracks (D, E), and isolated from any visible cracks [upper right Fe oxide in (F)]. (A) BSEM image of zircon RSES 80-10-8 (Pb-Pb age 3360 ± 9 Ma). (B) BSEM image of zircon RSES 80-9-20 (Pb-Pb age 3389 ± 5 Ma). (C) BSEM image of zircon RSES 86-4-18 (Pb-Pb age 4078 ± 7 Ma). (D) BSEM image of zircon RSES 82-1-5 (Pb-Pb age 3408 ± 36 Ma). (E) Cathodoluminescence image of grain in (C) with annealed crack circled. (F) BSEM image of zircon RSES 82-14-13 (Pb-Pb age 3342 ± 4 Ma). (G) Cathodoluminescence image of grain in (F). See Table DR4 for the Pb-Pb data for these zircons. Data acquired as part of the inclusion study by Bell et al. (2015).
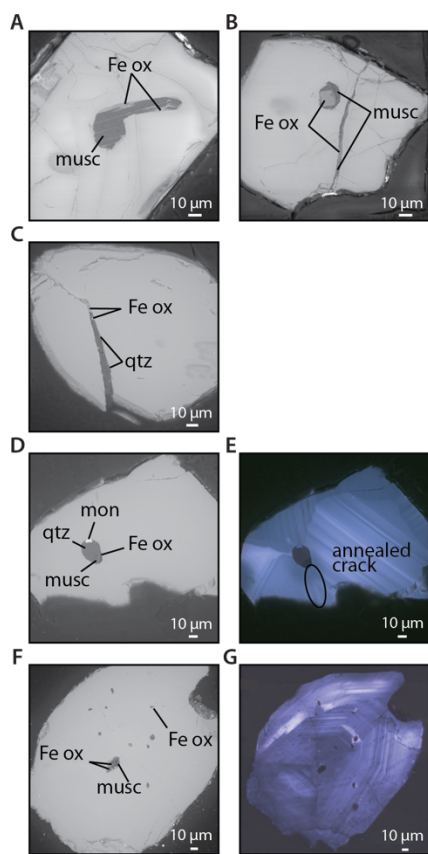
Table DR1. Preparation and measurement details for the sets of zircons analyzed in this study.

Set	Cleaning	Source	Mount	U-Pb?	Magnetization	N	Instrument	Other Analyses
1	Alcohol	RSES 199	Epoxy	Yes	Frantz IRM	257	QDM[2]	BSEM[3], CL[3], WDS[3]
2	Alcohol	RSES 57	Glass	No	Frantz IRM + 400 mT IRM[1]	10	SM[3]	Raman[4]
3	Alcohol	D175M-A1	Epoxy	No	NRM	8	QDM[2]	-
4	Alcohol	D175H-A1	Glass	No	NRM	60	SM[3]	-
5	0.5 N HCl for 2 h	D175M-A2	Epoxy	No	NRM	6	QDM[2]	-
6	0.5 N HCl for 20 h	D175M-A3	Epoxy	No	NRM	6	QDM[2]	BSEM[3], WDS[3]
7	6 N HCl for 12 min	D175M-B1	Epoxy	No	vertical IRM 400 mT	13	QDM[2]	BSEM[5], CL[5], EDS[5], X-ray[6]
8	6 N HCl for 1 h	D175M-B2	Epoxy	No	vertical IRM 400 mT	11	QDM[2]	BSEM[5], CL[5], EDS[5], X-ray[6]
9	6 N HCl for 12 min	D175H-A2	Glass	No	NRM	49	SM[3]	
10	Alcohol	RSES 80, 82, and 86	Epoxy	Yes	-	0	-	BSEM[7], EDS[7], CL[7], Raman[4]
11	None	D175C	Thin Section	No	vertical IRM 400 mT	5	QDM[2]	TL[3], BSEM[3]

Notes: The first column gives name of each zircon set, the second column lists how the zircons were cleaned, the third column lists the name of the zircon parent blocks, the fourth column lists the nature of the zircon mount (polished epoxy or drilled glass disk), the fifth columns lists whether the zircons were dated with U-Pb chronometry, the sixth column lists the form of magnetization analyzed [NRM = natural remanent magnetization, Frantz IRM = randomly-oriented near-saturation (up to 1.6 T) isothermal remanent magnetization from Frantz magnetic separator at ANU (see main text), IRM = isothermal remanent magnetization in MIT Paleomagnetism Laboratory], the seventh column lists the number of zircons analyzed magnetically, the eighth column lists the magnetometer used for the analyses (QDM = quantum diamond microscopy, SM = SQUID microscope), and the ninth column lists other analyses (BSEM = backscattered electron microscopy, WDS = wavelength dispersive spectroscopy, EDS = energy dispersive spectroscopy, CL = cathodoluminescence, X-ray = X-ray tomography, Raman = Raman spectroscopy), TL = transmitted light optical microscopy. For the CL data, only those of Bell et al. (2015) are shown in this study.

[1]The 400 mT IRM field was applied on zircons previously exposed to the Frantz magnetic separator. All zircons in set 2 were given this 400 mT IRM except for zircons 57-4-15 and 57-19-12. The 400 mT IRM field was applied to each zircon prior to mounting them in the glass disk, such that the magnetization directions of the zircons are expected to be randomly oriented after final mounting for SM analyses. The moments of these samples were then repeatedly measured during progressive thermal demagnetization conducted in air to 680 °C in using an ASC Scientific TD-48SC oven.
[2]Conducted at Harvard University
[3]Conducted at the Massachusetts Institute of Technology
[4]Conducted at the Geophysical Laboratory, Carnegie Institution of Science prior to thermal demagnetization
[5]Conducted at the University of Cambridge
[6]Conducted at Carl Zeiss X-Ray Microscopy, Inc.
[7]Conducted at the University of California, Los Angeles as part of the study by Bell et al. (2015). A total of 2,450 zircons were analyzed.

Table DR2. Statistics on locations of magnetization sources in zircons imaged with QDM.

Set	Cleaning	Pixel size (µm)/mode	Analyzed	Detected	Exterior-Only Sources	Interior Sources
1	alcohol	8.7 (low res)	257	147	122	25
1	alcohol	3.6 (hi res)	78	71	52	19
3	alcohol	7.3 (low res)	4	0	-	-
3	alcohol	4.8 (hi res)	6	5	3	2
5	0.5 N HCl for 2 h	4.8 (hi res)	6	5	3	2
6	0.5 N HCl for 20 h	4.8 (hi res)	6	4	3	1
7	6 N HCl for 12 min	4.8 (hi res)	13	6	2	4
8	6 N HCl for 1 h	4.8 (hi res)	11	8	2	6

Note: The first column gives name of each zircon set, the second column lists how the zircons were cleaned, the third column lists the QDM pixel size for each set of images (and denoting whether mode was low or high resolution), the fourth column lists the number of zircons analyzed, the fifth columns lists the number of zircons whose magnetizations were detected, the sixth column lists the number of zircons with exterior-only magnetization sources

(defined to be within ~20 µm of the zircons' rims), and the seventh column lists the number of zircons with interior magnetization sources.

Table DR3. Statistics of NRM intensity measured using the SM for sets 4 (non-acid-washed) and 9 (washed with 6 N HCl)

Set	Statistic	Value
4	Number of Zircons Measured	60
	Number of Zircons Detected	60
	Minimum NRM (Am^2)	2.17×10^{-14}
	Maximum NRM (Am^2)	4.34×10^{-12}
	Mean NRM (Am^2)	8.26×10^{-13}
	Median NRM (Am^2)	4.57×10^{-13}
	% Zircons with NRM $< 1 \times 10^{-13}$ Am^2	13.3
	% Zircons with NRM $> 1 \times 10^{-12}$ Am^2	23.3
9	Number of Zircons Measured	49
	Number of Zircons Detected	47
	Minimum NRM (Am^2)	$<\sim 1.0 \times 10^{-14}$
	Maximum NRM (Am^2)	5.15×10^{-12}
	Mean NRM (Am^2)	4.88×10^{-13}
	Median NRM (Am^2)	1.98×10^{-13}
	% Zircons with NRM $< 1 \times 10^{-13}$ Am^2	32.7
	% Zircons with NRM $> 1 \times 10^{-12}$ Am^2	12.2

Note: The first column gives identity of each zircon set, the second column lists the statistic, and the third column gives the value of the statistic.

Table DR4. Pb-Pb ages of set 1, 2, and 10 zircons.

Set	Zircon Name	^{207}Pb/^{206}Pb Age (Ma)	1σ Uncertainty (Ma)	% Discordant	Reference
1					Holden et al. (2009)
	RSES 199-1-4	4216	9.4	-2	
	RSES 199-1-15	4019	5.2	0	
	RSES 199-1-19	3977	4.9	5	
	RSES 199-2-16	4053	6.0	1	
	RSES 199-3-17	3954	9.0	147	
	RSES 199-3-19	4118	6.6	-2	
	RSES 199-4-16	3973	8.2	91	
	RSES 199-7-8	4101	10.7	-2	
	RSES 199-7-13	3975	5.0	-1	
	RSES 199-9-1	4056	5.8	-1	
	RSES 199-9-10	3982	5.6	95	
	RSES 199-9-17	3994	8.0	-1	
	RSES 199-10-2	4050	7.9	85	
	RSES 199-10-5	4036	13.5	3	
	RSES 199-12-7	4032	4.9	7	
	RSES 199-12-16	4100	6.6	0	
	RSES 199-13-2	4189	20.0	-3	
	RSES 199-13-17	4023	8.5	-3	
	RSES 199-14-3	4100	9.7	3	
	RSES 199-15-4	4117	5.6	-3	
	RSES 199-15-14	3970	9.2	23	
	RSES 199-18-19	4095	12.7	-3	
	RSES 199-19-20	4053	6.0	-4	
	RSES 199-20-3	4028	10.9	0	
	RSES 199-20-8	4083	5.3	5	
	All other RSES 199 zircons	<3900	-	-	
2					Holden et al. (2009)

RSES 57-1-3	4039	7.2	-1	
RSES 57-2-13	4016	5.5	-7	
RSES 57-3-19	<3900	-	-	
RSES 57-4-15	<3900	-	-	
RSES 57-6-19	<3900	-	-	
RSES 57-9-19	<3900	-	-	
RSES 57-15-11	4048	9.5	0	
RSES 57-19-12	4124	6.1	-5	
RSES 57-19-20	<3900	-	-	
10				Bell et al. (2015)
RSES 80-9-20	3389	5	1	
RSES 80-10-8	3360	9	27	
RSES 82-1-5	3408	36	9	
RSES 82-14-13	3342	4	2	
RSES 86-4-18	4078	7	-5	

Note: The first column gives name of each zircon set, the second column gives identity of each zircon, the third column lists the $^{207}Pb/^{206}Pb$ age, the fourth column gives the 1-standard deviation uncertainty on the $^{207}Pb/^{206}Pb$ age, the fifth column gives the concordance, calculated as $100 \times (t_{207/206} - t_{206/238})/t_{206/238}$, where $t_{207/206}$ and $t_{206/238}$ are the $^{207}Pb/^{206}Pb$ and $^{206}Pb/^{238}U$ ages, respectively, and the final column gives the reference for the Pb-Pb ages for each set of zircons.

Movie DR1. Animation showing X-ray tomography of 4019 ± 5 Ma Jack Hills detrital zircon RSES 199-1-15 (not acid-washed). Grain is viewed from different orientations and with differing density thresholds so that the interior and exterior of the grain become visible. Data were acquired with the ZEISS Xradia 520 Versa. Red voxels have high X-ray absorption relative to that of zircon host (grey) and are inferred to be Fe-rich particles. The movie shows that these high-absorption materials are confined to the exterior of the grain.

Supplementary References
Bell, E. A., Boehnke, P., Hopkins-Wielicki, M. D., and Harrison, T. M., 2015, Distinguishing primary and secondary inclusion assemblages in Jack Hills zircons: Lithos, v. 234-235, p. 15-26.
Berndt, T., Muxworthy, A. R., and Fabian, K., 2016, Does size matter? Statistical limits of paleomagnetic field reconstruction from small rock specimens: J. Geophys. Res., v. 121, p. doi:10.1002/2015JB012441.
Böhnel, H., Michalk, D., Nowaczyk, N., and Gonzalez Naranjo, G., 2009, The use of mini-samples in palaeomagnetism: Geophys. J. Int., v. 179, p. 35-42.
Bono, R. K., Tarduno, J. A., Dare, M. S., Mitra, G., and Cottrell, R. D., 2018, Cluster analysis on a sphere: Application to magnetizations from metasediments of the Jack Hills, Western Australia: Earth Planet. Sci. Lett., v. 484, p. 67-80.
Dare, M. S., Tarduno, J. A., Bono, R. K., Cottrell, R. D., Beard, J. S., and Kodama, K. P., 2016, Detrital magnetite and chromite in Jack Hills quartzite cobbles: Further evidence for the preservation of primary magnetizations and new insights into sediment provenance: Earth Planet. Sci. Lett., v. 451, p. 298-314.
de Faria, D. L. A., and Lopes, F. N., 2007, Heated goethite and natural hematite: Can Raman spectroscopy be used to differentiate them?: Vib. Spectrosc., v. 45, p. 117-121.
Fu, R. R., Weiss, B. P., Lima, E. A., Kehayias, P., Araujo, J. F. D. F., Glenn, D. R., Gelb, J., Einsle, J. F., Bauer, A. M., Harrison, R. J., Ali, G. A. H., and Walsworth, R. L., 2017, Evaluating the paleomagnetic potential of single zircon crystals using the Bishop Tuff: Earth Planet. Sci. Lett., v. 458, p. 1-13.

Glenn, D. R., Fu, R. R., Kehayias, P., Le Sage, D., Lima, E. A., Weiss, B. P., and Walsworth, R. L., 2017, Micrometer-scale magnetic imaging of geological samples using a quantum diamond microscope: Geochem. Geophys. Geosyst., v. 18, p. doi:10.1002/2017GC006946.

Holden, P., Lanc, P., Ireland, T. R., Harrison, T. M., Foster, J. J., and Bruce, Z., 2009, Mass-spectrometric mining of Hadean zircons by automated SHRIMP multi-collector and single-collector U/Pb zircon age dating: The first 100,000 grains: Int. J. Mass Spectrom., v. 286, p. 53-63.

Lima, E. A., and Weiss, B. P., 2016, Ultra-high sensitivity moment magnetometry of geological samples using magnetic microscopy: Geochem. Geophys. Geosyst., v. 17, p. doi:10.1002/2016GC006487.

Nasdala, L., Irmer, G., and Wolf, D., 1995, The degree of metamictization in zircon: a Raman spectroscopic study: Eur. J. Mineral., v. 7, p. 471-478.

Tarduno, J. A., and Cottrell, R. D., 2013, Signals from the ancient geodynamo: A paleomagnetic field test on the Jack Hills metaconglomerate: Earth Planet. Sci. Lett., v. 367, p. 123-132.

Tarduno, J. A., Cottrell, R. D., Davis, W. J., Nimmo, F., and Bono, R. K., 2015, A Hadean to Paleoarchean geodynamo recorded by single zircon crystals: Science, v. 349, p. 521-524.

Wang, H., Weiss, B. P., Bai, X.-N., Downey, B. G., Wang, J., Wang, J., Suavet, C., Fu, R. R., and Zucolotto, M. E., 2017, Lifetime of the solar nebula constrained by meteorite paleomagnetism: Science, v. 355, p. 623-627.

Weiss, B., 2017, Paleomagnetism of the Jack Hills rocks and zircons, 2017 MagIC Workshop: Earth's Magnetic Field from the Beginning: La Jolla, CA, p. https://www.youtube.com/watch?v=kyxExXdlLpc&t=1213s.

Weiss, B. P., Maloof, A. C., Harrison, T. M., Swanson-Hysell, N. L., Fu, R. R., Kirschvink, J. L., Watson, E. B., Coe, R. S., Tikoo, S. M., and Ramezani, J., 2016, Reply to Comment on "Pervasive remagnetization of detrital zircon host rocks in the Jack Hills, Western Australia and implications for records of the early dynamo": Earth Planet. Sci. Lett., v. 450, p. 409-412.

Weiss, B. P., Maloof, A. C., Tailby, N., Ramezani, J., Fu, R. R., Hanus, V., Trail, D., Watson, E. B., Harrison, T. M., Bowring, S. A., Kirschvink, J. L., Swanson-Hysell, N. L., and Coe, R. S., 2015, Pervasive remagnetization of detrital zircon host rocks in the Jack Hills, Western Australia and implications for records of the early geodynamo: Earth Planet. Sci. Lett., v. 430, p. 115-128.